JOURNAL OF GEOPHYSICAL RESEARCH, VOL. 103, NO. B3, PAGES 4915–4927, MARCH 10, 1998

Rate and state of background stress estimated from the aftershocks of the 1989 Loma Prieta, California, earthquake

Susanna Gross

Cooperative Institute for Research in the Environmental Sciences, University of Colorado, Boulder

Roland Bürgmann

Department of Geology, University of California, Davis

Abstract. Estimates of the tectonic stress state including loading rate and magnitude of background stress are derived from the spatial and temporal distribution of Loma Prieta aftershocks. This technique was previously applied to the Landers aftershock sequence [*Gross and Kisslinger*, 1997] and is based upon the seismicity model of *Dieterich* [1994]. Dieterich's theory suggests that background seismicity should be proportional to stress rate and the number of aftershocks in an area should be proportional to the stress step experienced in that area. We used two independently derived source models to compute the stress step from the mainshock and to determine how effective that stress step was in triggering aftershocks. A background stress state is then chosen which makes the stress steps at the aftershock locations most distinct from the stress steps at hypocenters of background seismicity. The best fitting background stress state has its greatest compressive stress plunging $\approx 17°$ to N13°E, and an intermediate stress very close in magnitude to the least principal stress. The small shear stresses at depth and low coefficient of friction suggest that high-pressure pore fluids may be present inside active faults. The estimated stress rate of ~ 70 Pa/d (0.25 bar/yr) is comparable to the stress rate found for the southern San Andreas Fault system. We found a best fitting "effective" coefficient of friction $\mu' \approx 0.2$ for the Loma Prieta area, significantly less than $\mu' \approx 0.6$ estimated for Landers in previous work. Variations in aftershock decay rate within the Loma Prieta aftershock zone are correlated with static stresses caused by postseismic slip as modeled by *Bürgmann et al.* [1997]. Some of the postseismic slip occurred on structures that did not slip during the mainshock, so the postseismic and coseismic stress step fields have different spatial distributions. The effectiveness of slowly accumulated postseismic static stresses in triggering aftershocks is especially interesting because dynamic stresses are insignificant in this case.

1. Introduction

The 1989 $M_W = 7.0$ Loma Prieta earthquake was a very educational event for the seismological community, illustrating the significance of seismic hazard from events that do not break the surface. Loma Prieta also raised some important questions relating to earthquake source mechanics because the aftershock focal mechanisms were so diverse that they suggested that slip on the mainshock had completely relieved homogeneous resolved shear stresses on the mainshock fault plane [*Michael et al.*, 1990]. Effectively zero shear stresses following the mainshock were unexpected because they imply very low dynamic coefficients of friction, which had not been observed in the laboratory. In combination with the modest stress drop, the low residual stresses on the fault plane also suggest that either the static coefficient of friction was quite low or the effective normal stress was much less than the overburden. Focal mechanisms cannot constrain the magnitude of the background stresses, so it is difficult to address these possibilities without more information.

One promising mechanism for producing low coefficients of both static and dynamic friction is the possible presence of pore fluids with very high fluid pressures. Since fluid pressures act on all the pore sur-

Paper number 97JB03010.
0148-227/98/97JB-03010$09.00

faces, they counteract much of the normal stress that would otherwise force the two sides of a fault together at depth, and they help to maintain the pore volume. Changes in normal stress could be balanced by changes in pore volume and associated changes in pore fluid pressure, reducing the effect of normal stress on fault friction. In order to have a significant effect, the pore fluids must have a pressure comparable to the lithostatic stresses that act at depth. A related hypothesis involves deformation of the rock mass as a whole. If crustal rocks deform like fluids, so that the strains are accommodated through permanent shape changes, then background shear stresses may be relieved aseismically. Smaller stresses are more easily canceled out by fault movement and could more easily produce the small residual shear stresses left on the Loma Prieta fault plane.

Reasenberg and Simpson [1992] used changes in the rate of seismicity on faults in the bay area to estimate the effective coefficient of friction μ' and found 0.2 fits the data best. A very low effective coefficient of friction is consistent with high-pressure pore fluids being present in fault zones, as discussed above, but the result might be influenced by some of the simplifying assumptions that Reasenberg and Simpson made in their modeling. They assumed that the seismicity occurred on right-lateral vertical strike-slip faults parallel to the major mapped faults in the area, and they also used a simple rectangular dislocation to represent the source. We have used the much more complicated source models published by *Beroza* [1991] and *Wald et al.* [1991] and have made a different assumption, i.e., that the seismicity occurred on fault planes which were optimally oriented with respect to a background stress field.

We address some of the questions raised in earlier studies of the Loma Prieta sequence by comparing the seismicity expected from various stress and fault friction models to the observed seismicity. This stress modeling technique was first applied to the aftershocks of the 1992 Landers earthquake [*Gross and Kisslinger*, 1997] and is based upon the seismicity theory of *Dieterich* [1994]. The technique produces estimates of the background stress state including the effective normal stress, the coefficient of fault friction, the rate of tectonic loading, and the Dieterich friction parameter A_D. We have also directly addressed the relationship between aftershocks and the postseismic relaxation process by studying the effects of the postseismic stress field upon the aftershocks. The Loma Prieta event is especially well suited to studies of postseismic relaxation because of extensive observations of the relatively large and well-constrained signal. The postseismic relaxation did not occur solely on the fault which generated the mainshock [*Bürgmann et al.* 1997], and so it is possible to distinguish the effects of stress transfer from postseismic slip from the delayed effect of coseismic slip. We find that those portions of the Loma Prieta aftershock zone that were loaded postseismically exhibit faster aftershock decay, a relationship expected from *Dieterich's* [1994] seismicity theory.

If *Dieterich's* [1994] model of seismicity is correct, then the techniques we present could be used to estimate loading rates for active fault zones with well-established seismic networks. When such a network records the aftershock sequence of an event whose slip distribution has been well constrained, the response of the local fault network to stresses can be calibrated, and loading rates can be estimated. In combination with strain rates, stress rates can constrain the extent to which aseismic processes are releasing crustal strains. Loading rates are most useful in seismic hazard work because they can directly measure the accumulation of elastic energy which drives infrequent large earthquakes.

2. Data

The seismicity data used in this work are from the California Seismic Network (Calnet) catalog [*Hill et al.*, 1991]. We use events having horizontal errors < 1 km, rms misfits < 0.15 s, at least five phase arrivals picked, and the largest gap in azimuths of stations about the epicenter $< 91°$. These restrictions are identical to those customarily used to define quality "A" locations [*Lee and Lahr*, 1975] except that we have dropped the restriction that events be within one source depth of the closest seismic station. We relax the depth restriction because we want to reduce spatial inhomogeneities in completeness and not to artificially reduce the reporting rate for shallow events in the final catalog. We apply a spatial cut to the catalog, using only events north of 36.5°N, south of 37.5°N, east of 122.5°W, and west of 121°W. After applying these cuts, the working catalog has more than 43,000 events occurring between 1978 and 1992. The catalog includes more than 13,000 events after the mainshock, so there are enough events to well define the spatial distribution of seismicity both before and after the mainshock.

Several catalog subsets are defined so that spatial variations in the stress state and rate can be explored. Northern and southern subsets are defined to be those events north or south of 37°N latitude. The Calaveras Fault subset includes events east of a line running from 37.3°N, 121.9°W through 36.95°N, 121.5°W. The San Andreas subset is defined to be those events west of the same line. These roughly equal divisions of the catalog are designed to provide both tectonically interesting and reasonably well constrained stress inversions.

The modeling results presented in this paper use the seismic source models for the Loma Prieta mainshock published by *Beroza* [1991] and *Wald et al.* [1991]. Both models of slip during the mainshock are derived from strong motion waveform inversions, but the *Wald et al.* [1991] model also includes some teleseismic waveforms. The source models are an essential element of the technique because they define both the spatial distribution

of the stress change and the magnitude of the stress step due to the mainshock, which together calibrate the seismic response of the faults in the area to stress and constrain the magnitude of background stress and stress rate. Two models of the mainshock source are used in order to estimate the magnitude of uncertainties in stress state and rate due to variations in the seismic source.

3. Analysis Techniques

3.1. Stress Modeling

We use the stress modeling technique first applied by *Gross and Kisslinger* [1997], in which the stress step from the mainshock is used to compute failure stress. The background stress state is fit to the spatial distribution of seismicity. Free parameters defining the background stress are chosen to maximize the statistical significance of the difference between stress steps averaged over hypocenters of aftershocks and stress steps averaged over hypocenters of background seismicity.

Stress decreases are expected to suppress seismic activity, and stress increases are expected to enhance it. The failure stress σ_F on optimally oriented planes is computed from the principal stresses σ_i (including background stresses) and the effective coefficient of friction μ', which includes the effects of fluid pressure P_f,

$$\sigma_F = \left(\sqrt{\mu'^2+1}\right)\left\{\frac{\sigma_1-\sigma_3}{2}\right\} - \mu'\frac{\sigma_1+\sigma_3}{2}. \quad (1)$$

This expression for σ_F, derived in the appendix, is similar to the Coulomb failure function or CFF [*Reasenberg and Simpson*, 1992; *King et al.*, 1994; *Harris et al.*, 1995; *Nostro et al.*, 1997], with the only significant difference being that we consider oblique slip while computing the failure function on optimally oriented fault planes. We have adopted this notation to avoid the incorrect implication that the definition of failure stress involves an assumption of Coulomb friction. The failure stress is a weighted sum of maximum shear and normal stress and has no implication that the friction must be independent of stressing history, as Coulomb friction is. Expression (1) is for the maximum failure stress obtainable on faults in any orientation in three dimensions and also allows slip in any direction on those faults, so it implicitly assumes that fault planes exist in a wide variety of orientations and that their frictional properties are not a function of orientation. Changes in failure stress $\Delta\sigma_F$ are found for each hypocenter by subtracting σ_F without the mainshock stress step from σ_F with it, $\Delta\sigma_F \equiv \sigma_F^{\text{total}} - \sigma_F^{\text{background}}$.

The best fitting effective coefficient of friction μ' is not the same as the intrinsic friction measurable in the laboratory μ because intrinsic friction coefficients are the ratio of total shear τ to effective normal stress $\sigma - P_f$ necessary to initiate slip on a surface. The effective coefficient of friction μ' is also not equivalent to the apparent coefficient of friction $\mu^* = \tau/\sigma$ of *Hill* [1993] because μ' is equal to the local slope of the failure envelope and sensitive to changes in pore pressure that may accompany steps in normal stress. If pore fluid pressure is a significant fraction of the lithostatic overburden and unaffected by the stress step from the mainshock, the apparent coefficient of friction μ' should be similar to intrinsic friction μ and much greater than the apparent coefficient of friction μ^*. If pore fluids change in pressure by an amount identical to the step in normal stress, then there will be no effective change in normal stress on the fault, and the effective coefficient of friction μ' will be zero.

The stress state fits presented here are different from most stress inversions because they are not based on focal mechanisms or magnitudes, only on hypocenters. Complete earthquake catalogs are not needed, only consistent monitoring and accurate locations. The technique could be adversely affected by changes in the network occurring at the time of the mainshock and cannot be applied to data from aftershock deployments. No assumptions about homogeneous structure, moment release, or statistical independence of earthquakes are required. The technique uses the locations of aftershocks to constrain the spatial distribution of the stress change, so accurate locations are important, especially near the mainshock source. The aftershocks are compared with background seismicity in order to correct for inhomogeneities of the structure. The background stress field is assumed to vary only with depth, but fairly minor modifications to the technique would allow this assumption to be relaxed. Similarly, the effective friction on the faults is assumed to be uniform. The stress state modeling is not greatly dependent upon details of the friction model, but it does assume that seismicity rate is some monotonically increasing function of changes in failure stress $\Delta\sigma_F$.

3.2. Fitting Statistic

To quantify the fit of stress step to the spatial distribution of seismicity, we compute

$$\mathbf{t} = \frac{\overline{\Delta\sigma_F^{\text{before}}} - \overline{\Delta\sigma_F^{\text{after}}}}{\sqrt{s^2_{\text{before}}/N_{\text{before}} + s^2_{\text{after}}/N_{\text{after}}}}, \quad (2)$$

where the symbol s is used to represent the standard deviation of a set of $\Delta\sigma_F$ values, N is the number of events in the set, and $\overline{\Delta\sigma_F^{\text{before}}}$ is the average change in failure stress evaluated at hypocenters of background events. The $\mathbf{t}$ statistic is computed from the seismicity from each of eight spherical shells shown in Figure 1. The summary statistic $\Sigma_{i=1}^{8}\mathbf{t_i}$ is defined to be the sum of the $\mathbf{t}$ statistics from the eight spherical shells, and it is this summary statistic which is used to select the best fitting model.

The $\mathbf{t}$ statistics used to quantify the fit of the seismicity to the stress field are quite different from the β

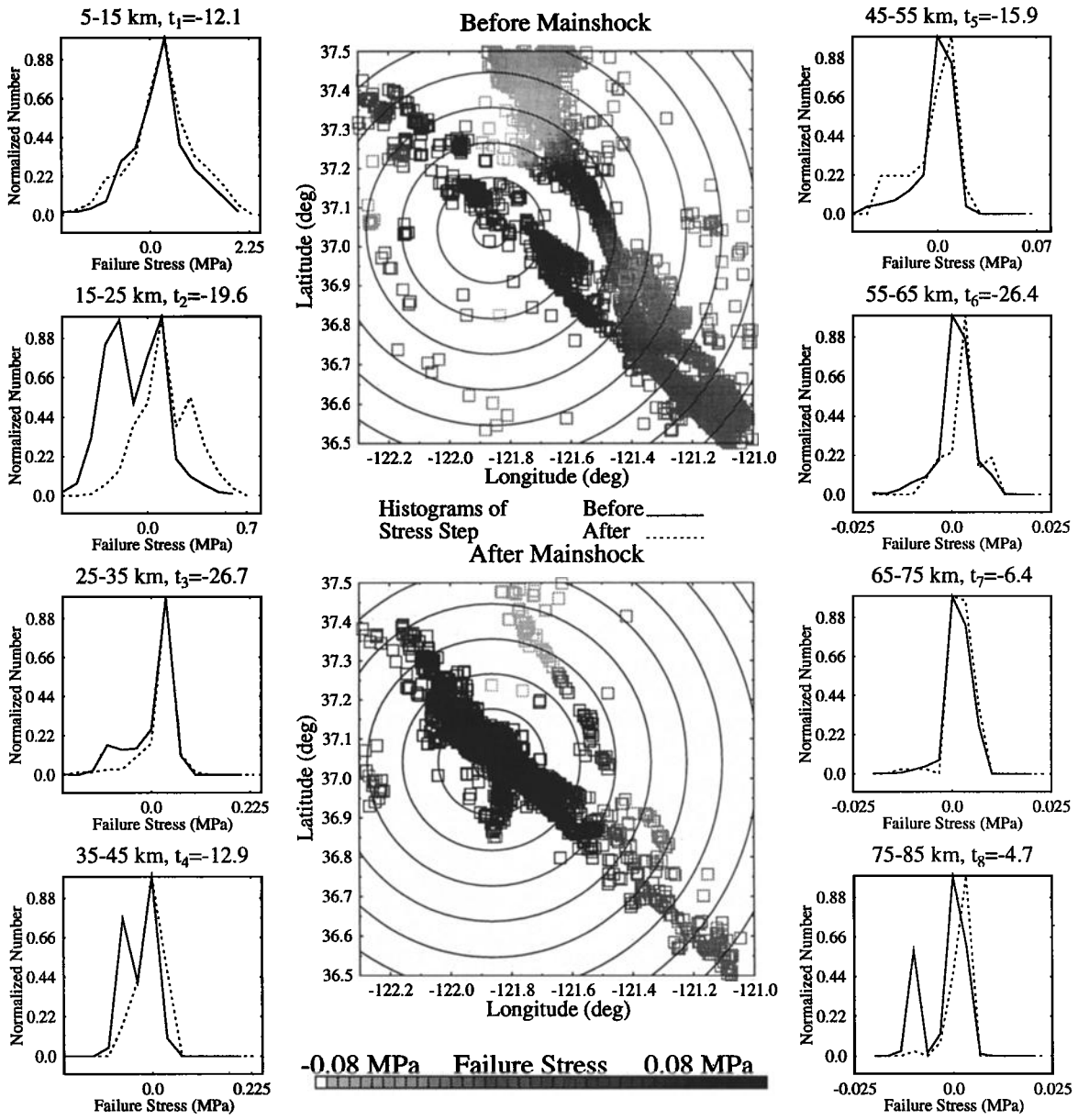

Figure 1. (middle) Seismicity in map view, with darker shading indicating increases in failure stress for the model listed in the first row of Table 1. (left) and (right) The solid and dotted lines on the small histograms illustrate the distributions of change in failure stress on optimally oriented planes, $\Delta\sigma_F$ for seismicity taken from different distance ranges surrounding the hypocenter of the Loma Prieta mainshock before and after the mainshock. **T** statistics are computed for each distance range to test how well the change in seismicity correlates with the change in stress, and those **t** statistics are summed to evaluate the models. Thousands of models are compared by computing **t** statistics for each one.

statistic used by *Reasenberg and Simpson* [1992]. The β statistic is a measure of the significance of the seismicity rate change in a fairly small region which is presumed to have a uniform stress step acting upon it. It is suitable for making maps of rate change, but less useful for quantifying the relationship between the seismicity and stress in a highly variable three-dimensional stress field. The **t** statistic approach is more similar to a cross-correlation, in which the change in spatial distribution of seismicity is compared directly with the stress change field, with few spatial bins and only two broad time categories defined. Since the β statistic is derived from a Poisson process in time, it requires a declustered catalog. The **t** statistic is fairly resistant to temporal clustering, since it does not assume Poisson statistics and averages over large spatial volumes, but it does summarize the distributions of stress change with the mean and variance, quantities that would be more applicable to Gaussian distributions than they are to the true distributions of $\Delta\sigma_F$ shown in Figure 1. Since the **t**

statistic is designed to quantify changes in the mean of a distribution, it detects increases in average $\Delta\sigma_F$, not only changes in sign.

Each stress state is defined by giving the orientations of the principal stresses in terms of the azimuth (az) of the most compressive principal stress (σ_1) (Table 1), the plunges (pl) of the greatest and least principal stress, and the ratio of stress magnitudes ϕ

$$\phi = (\sigma_2 - \sigma_3)/(\sigma_1 - \sigma_3). \quad (3)$$

The magnitude of the greatest principal stress is taken positive in compression and is an effective stress, including the effects of pore pressure. The remaining parameters are the effective coefficient of friction μ', (Table 1 and equation (1)), and the effective overburden density ρ', which controls how quickly the vertical effective normal stress increases with depth. The table also lists τ, the shear stress resolved onto the mainshock fault plane. Table 1 also gives the summary statistic Σt, which is the measure used to define how well the models fit in relation to one another. The more negative the number, the better the fit, but direct comparisons of summary statistics can only be made between models of the same catalog.

To find the best model, we compute summary t statistics for 10,000 models, choosing cases increasingly similar to the best so far. The models are evaluated in 10 groups of 1000 each. The initial group of models is uniformly and randomly distributed over the physically reasonable range for parameters having bounded ranges and exponentially distributed over the ranges of parameters having semi-infinite ranges. Trial background stress magnitudes are uniformly distributed in logarithm of stress, ranging from 1 MPa to 1 GPa. After the first 1000 models have been evaluated, later groups of models are drawn from triangular or exponential distributions centered upon the best model found so far. The widths of the distributions narrow progressively as the optimization progresses, until the final set of models involves small adjustments to the parameter values.

3.3. Dieterich Seismicity Model

If a population of faults loaded by a long-term steady tectonic stressing rate $\dot{\sigma_F}$ and normal stress σ, so that it produces a rate of background seismicity r, is subjected to a step in stress $\Delta\sigma_F$, the new seismicity rate n will follow the following function of time t [*Dieterich*, 1994]:

$$n = \frac{r}{\left[\exp\left(\frac{-\Delta\sigma_F}{A_D\sigma}\right) - 1\right]\exp\frac{-t}{t_a} + 1}. \quad (4)$$

A_D is a unitless parameter scaling the direct effect of velocity upon friction, and

$$t_a = \frac{A_D\sigma}{\dot{\sigma_F}} \quad (5)$$

is the time at which the sequence approaches the steady background rate of activity. If the aftershock rate is averaged over the duration of the aftershock catalog T which is short compared to the interseismic period, the average rate of aftershocks $\bar{n}$ can be shown [*Gross and Kisslinger*, 1997] to be linearly proportional to the stress step $\Delta\sigma_F$,

$$\frac{\bar{n}}{r} \approx \frac{\Delta\sigma_F}{T\dot{\sigma_F}}. \quad (6)$$

Two crucial properties of the Dieterich seismicity model used in this work are the linear proportionality between the steady state rate of seismicity and background stress rate and a similar linear proportionality between the number of aftershocks and the stress step. Both relationships are applied to changes in seismicity rate at a given location instead of variations in seismicity rate between locations. In this way, regional variations in fault structure and density are accounted for. The two crucial properties of Dieterich seismicity represent assumptions on which the estimates of stress rate presented below are based. Other friction relations consistent with these assumptions are also consistent with the stress rate estimates.

At $t << t_a$, the Dieterich aftershock decay function reduces to a form very similar to the modified Omori model,

$$n = \frac{K}{(t+c)^p}, \quad (7)$$

except that the Dieterich model has $p = 1$. In (7), K scales the total number of aftershocks, c is a time shift that removes the singularity at $t = 0$, and p, which is typically between 0.5 and 2, controls the rate of de-

Table 1. Stress State and Fault Friction Fits

Region	Σt	σ_1 az	σ_1 pl	σ_1 mag, MPa	σ_3 pl	ϕ	μ'	ρ'	τ MPa
Whole catalog	-124	13	17	2.5	40	0.04	0.29	0.28	0.85 MPa
Uncertainties	±5.2	±6.3	± 12	± 1.6	± 29	± 0.14	± 0.12	± 0.49	-
Northern half	-72	34	-8	6.9	-41	0.22	0.26	1.64	2.64
Southern half	-118	16	29	5.8	-5	0.89	-0.20	-1.10	2.03
Calaveras Fault	-34	25	-5	2.4	4	0.98	-0.38	-0.14	0.46
San Andreas Fault	-73	25	9	2.6	-11	0.04	0.04	0.17	0.98
$M_L > 1.5$	-57	29	-6	5.6	0	0.10	0.55	0.64	0.38
Wald source	-117	22	-6	1.5	4	0.04	-0.06	0.16	1.08
Depth< 6.5km	-95	30	4	4.0	-39	0.06	0.98	0.60	2.43
Depth> 6.5km	-116	19	17	2.3	40	0.42	0.10	-0.02	0.82

cay. Another function that has been successfully used to model aftershock decay is the stretched exponential [*Kisslinger*, 1993],

$$n(t) = qN^* \frac{1}{t}\left(\frac{t}{t_0}\right)^q \exp[-\left(\frac{t}{t_0}\right)^q]. \quad (8)$$

There are two parameters controlling the rate of decay of the stretched exponential, t_0, the characteristic time, and q, a unitless power of the decay with a typical value of 0.4. N^* represents the total number of events the sequence will produce as $t >> t_0$. The modified Omori and stretched exponential functions will be used later to quantify variations in aftershock decay, and the Dieterich decay function will be used to estimate the friction parameter A_D.

3.4. Aftershock Decay Modeling

A practical technique for fitting and comparing aftershock models having a variety of functional forms has been developed [*Gross*, 1996; *Gross and Kisslinger*, 1994; *Kisslinger*, 1993; *Ogata*, 1983]. This technique finds the best fitting model by minimizing the Akaike information criterion (AIC), which also maximizes the likelihood of the model given the data.

For an aftershock model having n_p free parameters and a modeled rate $n(t_i)$, as a function of the time of the ith aftershock, the AIC is

$$\min(\mathrm{AIC}) = 2N - 2\sum_{i=1}^{N} \max[\log(n(t_i))] + 2n_p, \quad (9)$$

where N is the total number of aftershocks observed. The three models fit in this work (equations (4), (7), and (8)) all have $n_p = 3$ free parameters. The minimization is carried out by using the technique described by *Gross* [1996]. The lowest minimum from a series of 20 downhill simplex runs is selected, with each run started from a different, randomly selected set of initial parameters. The last 10 runs are started progressively closer to the best value found so far.

4. Results

4.1. Stress State

Table 1 lists the best fitting background stress states and coefficients of friction for different catalog subsets and source models. With the exception of the Calaveras subset, the stress state fits listed in Table 1 are fairly similar to one another. The greatest principal stress directions are all NNE with magnitudes of 1.5 to 7 MPa, with small values of the stress ratio ϕ. The coefficients of friction are most often less than those observed in rock friction experiments, ranging from -0.4 to 1.0, and the effective overburden densities are much less than the true densities of crustal rocks.

It is difficult to develop a measure of statistical uncertainty for fits to data that are not statistically independent. One measure of uncertainty which includes variations in the data and source model, as well as the fitting procedure, is the variation in fitted parameters between the different cases listed on Table 1. To derive an estimate of the uncertainty inherent in the fits, we fit background stresses to a series of perturbed catalogs. These catalogs are constructed from the whole catalog, but with some clusters of background and aftershocks duplicated or omitted. All background events within 10 days and 10 km of each other are linked into clusters, but the distance and time thresholds for clustering of the aftershocks decrease as the third power of distance from the source. A set of 100 perturbed catalogs is constructed by selecting clusters and single events with equal probability. Stresses were fit to the perturbed catalogs using the same technique applied to the original data, and variations in best fitting parameters are reported in Table 1.

4.2. Comparisons With Previous Results

Those fit parameters listed in Table 1 which exhibit the smallest degree of variability between fits using different catalog subsets and source models are the fitting parameters which most often agree with the results of stress inversions using different methods. Perhaps the most stable result is the azimuth of the greatest principal stress. *Amelung* [1996] used *Kostrov's* [1974] method of summing the moment tensors of events to examine the seismic strain field in the bay area and found strain states consistent with Table 1. He determined orientations of the strain axes for the combined pre-1989 and post-1989 catalog. An area centered around the Loma Prieta epicentral region shows d_1, the axis of maximum shortening, oriented at about N19°E. On the San Francisco peninsula, north of Loma Prieta, he finds d_1 to be oriented $\sim$ N30°E; south of Loma Prieta, in the Hollister area, he determines an azimuth of about N4°E. Along the southern Calaveras fault, d_1 is oriented about N15°E in this inversion. Using 53 preearthquake focal mechanisms near the epicentral region, *Amelung* [1996] finds d_1 to be oriented about N25°E.

Michael et al. [1990] inverted focal mechanisms from before and after the 1989 Loma Prieta earthquake to infer the coseismic stress changes. A stress tensor inversion of 304 events in the Loma Prieta epicentral region that occurred from 1969 to 1989 suggests a relatively homogeneous stress field with a N-S most compressional stress axis and subvertical intermediate stress axis [*Michael et al.*, 1990]. In the immediate vicinity of the earthquake rupture, their result shows that σ_1 is oriented N8°E and σ_2 is subvertical, similar to the whole catalog inversion shown in Table 1. South of 37° latitude, *Michael et al.* [1990] found a relatively homogeneous background stress field with N-S compression and a vertical intermediate stress axis, less consistent with our results. For both regions they found $\phi = 0.39$, significantly different from our results.

Reasenberg and Simpson [1992] computed the static stress changes from the Loma Prieta earthquake and compared them with changes in microseismicity rate. Since their modeling approach is similar to ours, it is reassuring that they also found that a low coefficient of friction (0.2) produces the best model and shows a significant correlation between stress and seismicity rate changes.

Previous estimates of the magnitude of the background stress are somewhat larger than the background stresses in Table 1, which result in shear stresses resolved onto the mainshock fault plane ranging from 0.4 to 2.7 MPa (Table 1). On the basis of a mechanical model of the effects of the coseismic rupture on the orientation of the strain axes, *Amelung* [1996] suggests that the background shear stress was less than 25 MPa. *Michael et al.* [1990] and *Zoback and Beroza* [1993] argue that the stress drop on the mainshock fault plane was nearly complete. This suggests a background magnitude of shear stress of about 5 MPa and near lithostatic pore pressures [*Zoback and Beroza*, 1993].

4.3. Stress Rate

To estimate the background stress rate, we compute stress changes $\Delta\sigma_F$ from models of the Loma Prieta mainshock at the hypocenters of 10,000 aftershocks and 10,000 events representing background activity for the catalog subsets in Table 2. Each earthquake is classified into one of 20 categories on the basis of the modeled stress step $\Delta\sigma_F$ at the hypocenter; the categories are chosen so that there are 500 aftershocks in each category, all with similar stress steps. The number of background events n_{before} is not evenly distributed between bins, because background events are more common in regions of smaller $\Delta\sigma_F$ than aftershocks are. We then divide the number of events in the background and aftershock periods by the durations T of the respective periods to compute rates of activity and take a ratio of aftershock rate to background rate to find the aftershock amplification ratio for each stress category:

$$\frac{n_{\text{after}}}{n_{\text{before}}}\frac{1/T}{1/T_{\text{before}}} = \frac{\bar{n}}{r}. \tag{10}$$

As Figure 2 shows, the stress step $\Delta\sigma_F$ corresponds to a strong variation in aftershock amplification ratio, $\bar{n}/r$. Equation (6) may be solved for $\dot{\sigma_F}$,

$$\dot{\sigma_F} = \frac{r}{\bar{n}}\frac{\Delta\sigma_F}{T}, \tag{11}$$

Table 2. Shear Stress Rates With Uncertainties

	Linear Fit	L1 Norm
Whole catalog	129 ± 23	93
M_L >1.5	73 ± 1.6	73
Northern half	229 ± 37	146
Southern half	46 ± 2	48
Calaveras	113 ± 14	107
San Andreas	149 ± 25	84
Wald source	294 ± 62	195

Stress rate in Pa/d.

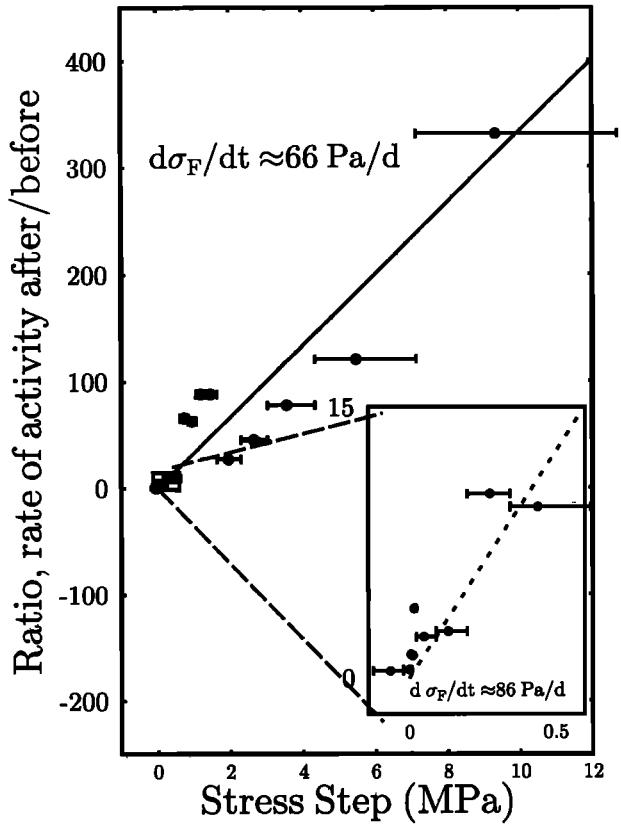

Figure 2. Fits of the aftershock amplification factor versus stress step for the first model in Table 1 with estimates of stress rate derived from the slope. The inset plot shows points near the origin. An outlier at 19 MPa with an amplification factor of 331 not shown on the plot influences the least squares fit in Table 1 more than the L1 norm fit.

to show that the stressing rate should be equal to the inverse of the slope of the line on the plot times the duration of the aftershock time interval T = 455 days for this catalog. Estimates of stress rate in Table 2 are found by doing least squares fits to the amplification factor versus stress step for the listed catalog, source model, and background stress. We also fit the slope using an L1 norm, which produced the estimates listed in Table 2. These robust fits generally show greater stability, but they also do not offer a misfit measure that can be interpreted as easily as the least squares fits.

The stress rate fits shown in Table 2 vary considerably, with the strongest contrast between the northern and southern subsets. The area near the creeping section of the San Andreas Fault shows much slower accumulation of stress than the rest of the region. The next most significant effects are source models and the magnitude cut, which produce fluctuations of almost a factor of 2 in loading estimates. The variation in stress rates found for the two different source models can only partially be explained by the 20% difference in total moment between the models and may partly be due to the

smoother distribution of slip directions in the *Wald et al.* [1991] model. The magnitude cut affects the stress rate by correcting for incomplete reporting of the early aftershocks, and so the case with $M_L > 1.5$ is probably the most dependable stress rate Table 2.

In order to place the stress rate estimates in a tectonic context, it is useful to compare them with previously reported strain rates for the area. *Lisowski et al.* [1991] provided an excellent summary of California trilateration data, showing strain rates across the San Andreas and Calaveras faults recorded by the Monterey Bay and San Francisco Bay networks. The southern part of the Monterey Bay network is well modeled by rigid block motion with the only off-fault strain occurring in the sliver of crust between the two faults. The northern half of the network is less well constrained but shows roughly 20 mm/yr displacement over 35 km. This translates into a stress rate of 50 Pa/d using a shear modulus of 3×10^{10} Pa. This stress rate is slightly smaller than most of the numbers reported in Table 1, most resembling the stress rate computed from the catalog of events $M_L > 1.5$. Since the seismic stressing rate is large enough to account for all the strain being accumulated, the estimates suggest that there is little anelastic deformation occurring in the area, apart from the creep on the San Andreas and Calaveras which is evident in both the trilateration data and the lower stress rate found for the southern catalog subset.

4.4. Postseismic Relaxation

Table 3 lists three different decay parameters fit to nine subsets of Loma Prieta aftershocks and also reports the ratio of the number of aftershocks to number of background events in each subset. The subsets are defined with respect to the postseismic stress step $\Delta\sigma_F^P$, which is the change in failure stress due to the postseismic slip as modeled by *Bürgmann et al.* [1997] and shown in Figure 3. This model suggests postseismic oblique reverse slip on the rupture and shallow thrust faulting NE of the San Andreas Fault. The postseismic slip did not all occur on the mainshock source plane,

Table 3. Aftershock Decay Measures for Subsets

Postseismic	t_0	q	p	t_0^q	n_a/n_b
Coseismic $\Delta\sigma_F > 1.84$ *MPa*					
$\Delta\sigma_F^P > 1$ kPa	26.3	0.44	1.15	4.2	∞
1 kPa $> \lvert\Delta\sigma_F^P\rvert$	56.5	0.37	1.12	4.5	7.7
-1 kPa $> \Delta\sigma_F^P$	48.4	0.47	1.09	6.2	30
1.84 MPa $> \Delta\sigma_F >$ *155 kPa*					
$\Delta\sigma_F^P > 1$ kPa	33.8	0.35	1.01	3.4	16
1 kPa $> \lvert\Delta\sigma_F^P\rvert$	18.7	0.44	1.01	3.60	9.6
-1 kPa $> \Delta\sigma_F^P$	16.1	0.47	1.31	3.65	5.6
1.55 kPa $> \Delta\sigma_F$					
$\Delta\sigma_F^P > 1$ kPa	138	0.76	3.00	41	1.4
1 kPa $> \lvert\Delta\sigma_F^P\rvert$	973	0.89	0.31	450	0.30
-1 kPa $> \Delta\sigma_F^P$	5.1×10^8	.65	0.36	4.7×10^5	0.28

Decay parameters were computed for events of $M_L >$ 1.3 for the cases with $\Delta\sigma_F <$1.84 MPa. Ten days of data after a large aftershock in the 1.84 MPa $> \Delta\sigma_F >$ 155 kPa sets were dropped.

so there are significant differences between the spatial distribution of the postseismic stress field and the coseismic stress step, differences that can be exploited in order to detect the effect of the postseismic stress field upon the aftershocks. Since we know that there is a strong relationship between aftershock generation and the coseismic stress step, the quantities to compare are the decay parameters and aftershock rates from those subsets for which the coseismic stress step was the same.

Table 3 gives values of the characteristic time t_0 of decay and the q value of the stretched exponential function (8)[*Kisslinger* 1993]. The third column gives the p value, the decay exponent from the modified Omori aftershock decay relation (7). All three parameters are fit using the maximum likelihood technique of *Gross* [1996]. Since there are two parameters controlling decay for the stretched exponential, we have combined them to make an overall measure of aftershock decay for the stretched exponential, which is given in Table 3. Large values of t_0^q and small values of p are associated with slow decay. The parameters in Table 3 show a tendency toward more rapid aftershock decay for those subsets that are loaded by the postseismic slip. There are 12 independent comparisons of values of p and t_0^q which can be made between subsets in the same $\Delta\sigma_F$ category, and 10 of these show the subsets with the greater postseismic loading decaying more rapidly, a correlation that should occur by chance

$$P = \frac{\Sigma_{i=0}^{2}\binom{12}{i}}{2^{12}},$$

or 2% of the time. The ratios of activity are also mostly in order, with an 11% probability of occurring by chance. Faster aftershock decay and greater numbers of aftershocks are expected for those subsets which are loaded postseismically on the basis of Dieterich seismicity theory, since the postseismic slip rate was greatest in the early part of the aftershock sequence. One especially interesting feature of this observed correlation between aftershock decay rates and postseismic loading is the absence of any dynamic effects from the postseismic slip. When seismicity is compared to static stresses generated by an earthquake, it is difficult to say for certain that the observed relationship could not have been created by some aspect of the dynamic stresses, which are short lived but larger in magnitude than the static stresses. Here we have an observable effect on aftershocks in a case for which dynamic stresses are negligible.

5. Discussion

The stress state and rate results presented above illustrate that the seismicity modeling technique is broadly consistent with previous models of the stress state, stress magnitude, fault friction, and strain rate for the Loma Prieta area. Collectively, these results suggest that the properties of Dieterich seismicity theory under-

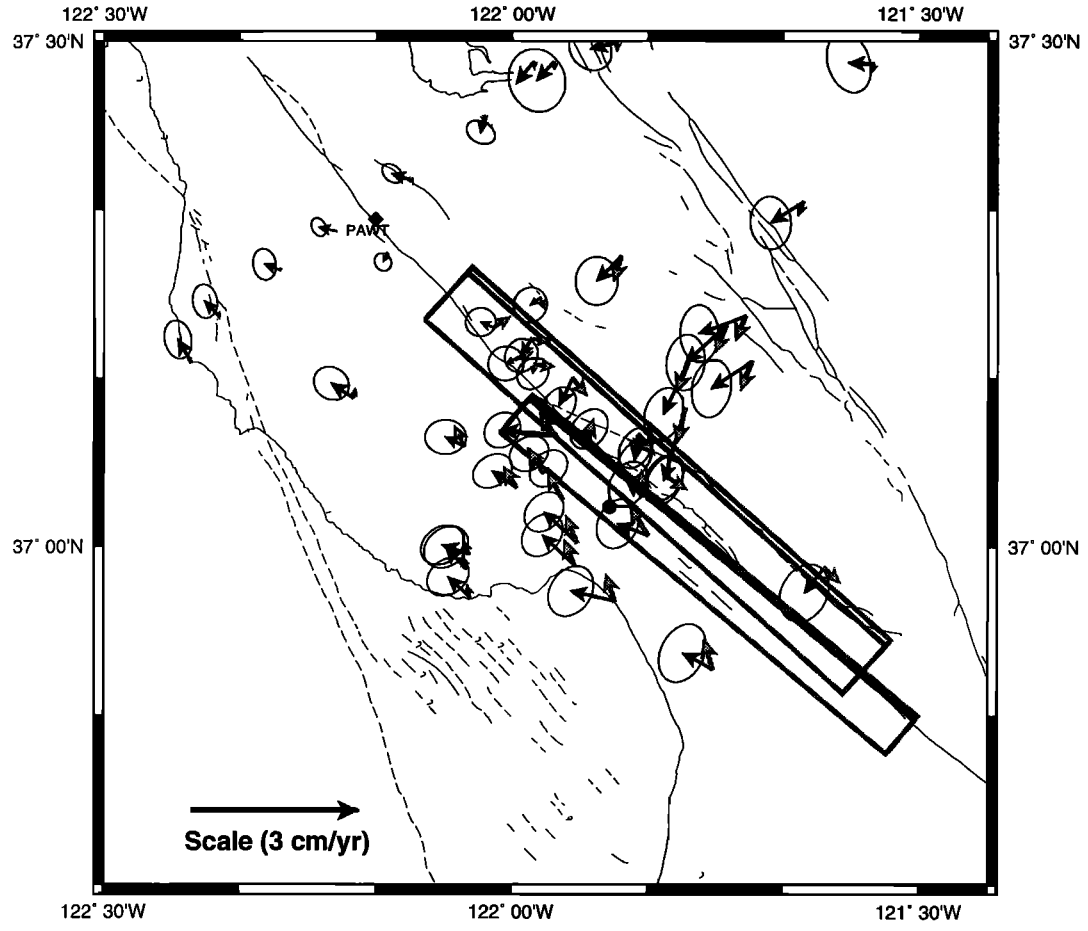

Figure 3. Postseismic velocity field from repeated GPS measurements in the southern San Francisco Bay area. Solid arrows with error ellipses on this plot represent the residual geodetic velocities, after the interseismic velocities have been removed. The shaded arrows are velocities from the postseismic model, which involves slip on the fault planes shown in rectangular map projection.

lying the modeling techniques are applicable to natural faults. The technique may provide information about the loading rate in areas where only seismicity data are available. The model also fits some quantities, like A_D and effective overburden density ρ', about which there is no independent information. Although the results are quite uncertain, they can be interpreted as consistent with high pore fluid pressures and relaxed lithostatic shear stresses.

The low principal stress magnitudes listed in Table 1 and also found for the Landers source region have interesting implications for crustal properties, if correct. The stress field computed with the seismicity model is the effective stress, because pore fluid pressures can counteract the effects of normal stresses, and the shear stresses are sensitive only to differences between principal stresses. This implies that the differences between the principal stresses at seismogenic depths are of order 3 MPa, but the overburden pressure at 6 km depth must be roughly 150 MPa, 50 times as large. Some process must be acting to reduce the shear stresses significantly, bringing the horizontal stresses into near equality with the vertical stresses, analogous to the isotropic stress tensor inside a fluid. One possible mechanism would be accumulated deformation of the crust, which could have occurred on a geologic timescale, permanently changing the shape of the crustal rocks and reducing shear stresses. A similar effect could be produced by near-lithostatic pore fluid pressure maintained over geologic time, but this would require seals inside the fault capable of resisting fluid pressure differences comparable to the difference between horizontal and vertical stresses on long timescales. High-pressure fluids also cause rocks to hydrofracture, forming systems of cracks that facilitate permanent shape change.

Employing the arguments of the previous paragraph, we can assume that the effective normal stress is approximately the size of the greatest principal stress as derived from the models. Our estimates of stress rate and the duration of the Loma Prieta aftershock sequence

made by fitting equation (4) (Figure 4) then permit a very rough estimate of the Dieterich friction parameter A_D to be made using (5), the definition of t_a,

$$A_D = \frac{t_a \dot{\sigma}_F}{\sigma} \approx 0.0037,$$

with a bestfitting value of $t_a = 170$ days and $\sigma \approx 3$ MPa. This estimate of A_D is close to the range of laboratory values, 0.005 to 0.012 [*Dieterich*, 1994]. If we take a much more narrowly defined spatial cut, including only those aftershocks which had a stress step greater than 295 kPa, then the best estimate for t_a, after correcting for the observed background rate, is 5082 days, giving $A_D \approx 0.11$. If we instead assume that the effective normal stress is comparable to the overburden pressure estimated above, the estimates for A_D range from 0.00007 to 0.0021, less than the laboratory values quoted above, which is a piece of indirect evidence for low effective normal stresses acting on the faults in the Loma Prieta source region.

Byerlee [1993] presented a model of mature fault zones such as the San Andreas, explaining the absence of a heat flow anomaly there and the low effective strength in terms of near-lithostatic pore pressures. In his model, the ambient pore pressures are assumed to be hydrostatic, and the shear stresses are much greater than typical earthquake stress drops. Elevated pore pressures are produced by the compaction of the gouge inside a fault zone which is divided into many compartments by impermeable seals. The sealing process occurs only on mature faults at depths below about 3 km where temperatures are high enough and occurs over an interseismic interval a few hundred years in duration. The seals are broken when an earthquake occurs. The sealing also prevents hydrofracture, which would otherwise occur when the pore fluid pressure exceeds the least principal stress.

The nearly isotropic stress tensors listed in Table 1 suggest an alternative explanation for elevated pore pressure in the fault zone. Principal stresses very similar to one another permit fluid-filled cracks of all orientations to be in hydrologic communication without causing hydrofracture or requiring sealing. Lithostatic pore pressures could be present outside of the fault as well and could have arisen from the lithification process or long-term compaction of the rock as a whole. Hydrologic seals would still have to be present in order to isolate the pressures characteristic of the different depths from one another, but they need not be formed and broken over short temporal and spatial scales. This model has the advantage of explaining low stress drops observed for small earthquakes on minor faults and on major ones after large events and predicts rather modest differences in failure strength between different faults resulting from factors such as geometry instead of fluid pressure. Because the total shear stress on a fault is small, it can be fairly readily counteracted by accumulated displacement, especially for more mature faults.

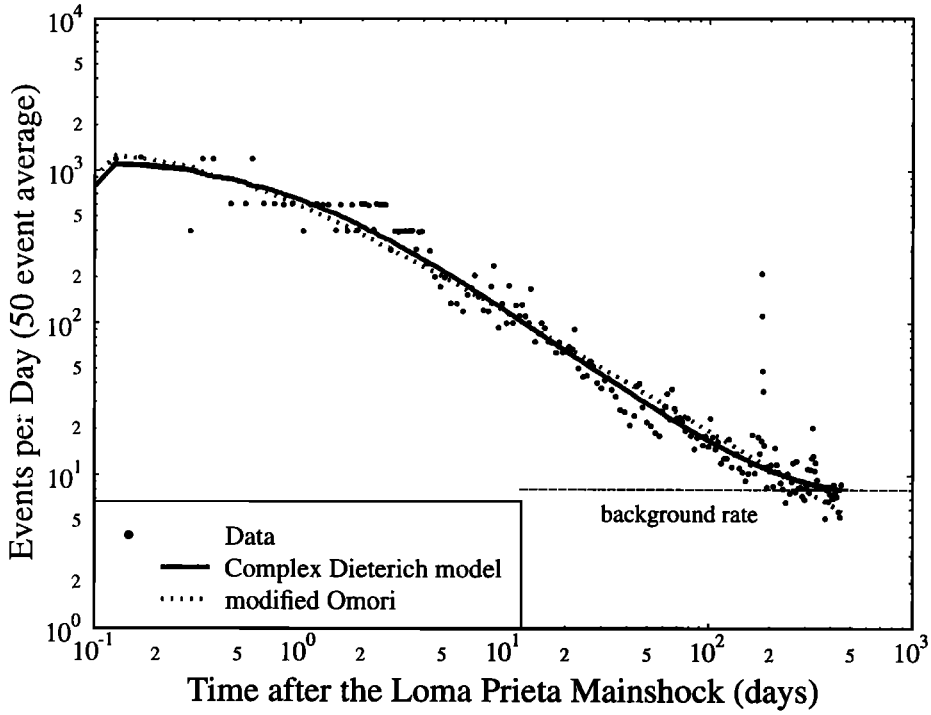

Figure 4. The rate of Loma Prieta aftershocks as a function of time with two aftershock decay models fit to the data. Time bins have been defined so that they each contain 50 events. The horizontal line represents a rate of activity estimated from the background period.

The effective density ρ' may be used to construct a very rough estimate of the total pore pressure P_f at depth,

$$P_f \approx (\rho - \rho')gh \quad (12)$$

and the pressures $P_s \approx \rho' gh$ which the fluid seals in faults would have to resist to sustain the pore pressure. Since the effective densities ρ' are generally much less than the true density of rock $\rho \approx 2700$ kg/m^3 and deformation could make the principal stresses similar to one another, the sealing pressure could be much less than the pore fluid pressure. If we take the shallow depth subset in Table 1 as typical for its estimate of $\rho' \approx 600$ kg/m^3, the maximum sealing pressure at 6.5 km depth is $P_s \approx 38$ MPa, attained when the pore fluid pressure reaches $P_f \approx 133$ MPa. The stress model listed in Table 1 for depths > 6.5 km has a negative effective density ρ', so the sealing pressure P_s should decline as depths increase beyond 6.5 km under that model. The pore pressure may increase slightly faster than the overburden below that depth. Low effective densities were also found for models of the Landers sequence [*Gross and Kisslinger*, 1997].

The low effective coefficients of friction listed in Table 1 and also found by *Reasenberg and Simpson* [1992] could have resulted from pore fluids confined to the faults, but there is some evidence in Table 1 that this effect is most significant at depths greater than 6 km. A higher coefficient of friction was also found in models of the much shallower Landers seismicity by *Gross and Kisslinger* [1997]. Mechanically, low coefficients of friction would be expected if the pore volume decreases in response to the increased normal stress and the pore fluid pressures act against this increase, increasing the pressure inside the crack nearly as much as the normal stress increases outside. Negative apparent friction coefficients could arise if the fluid pressure inside a fault actually increases faster than the normal stress, perhaps due to increased normal stress on cracks having a different orientation than the fault which are in hydrologic communication with the fault. This pore pressure increase would have to be maintained over the timescale during which most of the aftershocks occurred and only be strong enough to counteract normal stress changes due to the mainshock. Other symptoms of high pore pressure are the low effective overburden density and relatively long aftershock duration, which have already been discussed.

Some of the most interesting potential future applications of the modeling techniques we have employed for this work lie in the area of seismic hazard analysis. Stress rates estimated from seismicity may prove a better predictor of total moment release than strain rates, because strain is sometimes relieved through aseismic processes such as fault creep. Our observation of lower stress rates near creeping faults is an illustration of this effect, but it should in principle allow creep on buried faults to be detected as well. The stress rate analysis can be carried out using seismicity data alone for structures like off-shore faults for which strain data are difficult to obtain. The technique requires consistent long-term monitoring of seismicity before and after an event with a well-constrained slip distribution and numerous aftershocks. Dieterich seismicity theory in combination with stress-step modeling might improve our ability to forecast short-term hazards from the aftershocks of large events as well. This approach depends upon detailed seismicity data gathered by local and regional networks as well as a fairly well-constrained background stress state and rapid determination of the slip distribution for the mainshock. Serious application of these techniques to seismic hazards should not be attempted until additional verification and testing of the reliability of the modeling results has been carried out. Our study of the Loma Prieta aftershock sequence has been one such test.

6. Conclusions

The spatial distribution of Loma Prieta aftershocks is consistent with the model that static stresses from the mainshock triggered them and also implies a background stress that is consistent with local tectonics and observed strain rates. Best fitting models have the greatest effective stress of $\sim$ 1-7 MPa at a high angle to the fault plane, consistent with previous analysis of focal mechanisms [*Beroza and Zoback*, 1993].

The low magnitude of background stress and effective density much lower than true densities of rocks both suggest that high-pressure pore fluids are present. High pressure pore fluids also help explain the low effective coefficient of friction found for these models and how the relatively long duration of the aftershock sequence can be consistent with laboratory measurements of the constitutive parameter A_D.

The stress rate for the Loma Prieta area of 70 Pa/d (0.25 bar/yr) is somewhat less than the rate found for the southern San Andreas Fault system using Landers aftershocks but considerably greater than the rate found for seismicity south of 37°N latitude. This result is consistent with aseismic release of strain in the creeping section. The consistency of this result with known tectonics suggests that Dieterich seismicity theory is compatible with these observations.

Estimated values of the constitutive parameter A_D range from 0.0037 to 0.11 and are similar to laboratory values, but more experiments and estimates are needed. Smaller estimates of A_D result from the assumption of lithostatic effective normal stress. Correlation of the postseismic loading with aftershock decay rates supports the contention that static stresses trigger aftershocks.

Appendix: Derivation of σ_F

The failure function σ_F, shown on Figure 5, is the shear stress at which a failure envelope, assumed to be

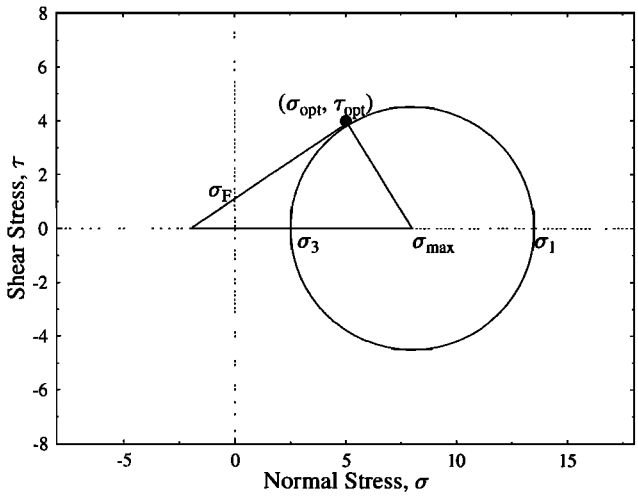

Figure 5. This cartoon of a Mohr's circle and linear failure envelope is used in the derivation of σ_F, the failure stress.

a line with slope μ', passes through the tau axis, where normal stress is zero. In the conventional representation, this intersection is written down in terms of $\tau_{\rm opt}$ and $\sigma_{\rm opt}$, which are the values of shear and normal stress (taken positive in compression) at the point where the failure line lies tangent to Mohr's circle. The failure line crosses the tau axis a distance $\mu'\sigma_{\rm opt}$ below $\tau_{\rm opt}$, so the failure stress may be written

$$\sigma_F = \tau_{\rm opt} - \mu'\sigma_{\rm opt}.$$

This formula has been presented by many authors [i.e., *Reasenberg and Simpson*, 1992; *King et al.*, 1994; *Harris et al.*, 1995; *Nostro et al.* 1997]. The difficulty with it is that the optimal orientation for failure generally must be found before $\tau_{\rm opt}$ and $\sigma_{\rm opt}$ can be evaluated. For the stress modeling presented in this paper, as well as *Gross and Kisslinger* [1997], a different formula is used. This other formula for σ_F is equivalent to the above formula, but is written in terms of the maximum shear stress $\tau_{\rm max}$ and the normal stress on planes of maximum shear, $\sigma_{\rm max}$, which can easily be evaluated,

$$\sigma_F = \sqrt{1+\mu'}\tau_{\rm max} - \mu'\sigma_{\rm max}.$$

This expression can be derived from the simple Mohr circle with a straight failure line having slope μ', shown on Figure 5. Consider the right triangle, formed by the failure line, the σ axis, and the radius which runs from the tangent point to the circle's origin. The hypotenuse of this triangle has a total length

$$\frac{\sigma_F}{\mu'} + \sigma_{\rm max},$$

because the triangle extends a distance σ_F/μ' beyond the τ axis. The circle radius is equal to $\tau_{\rm max}$, so the sine of the angle between the failure line and the horizontal axis can be written

$$\sin\alpha = \frac{\tau_{\rm max}}{\sigma_F/\mu' + \sigma_{\rm max}}.$$

The failure line has slope μ', so the sine of the angle it makes with with a horizontal line is

$$\sin\alpha = \frac{\mu'}{\sqrt{1+\mu'^2}}.$$

Substituting this into the previous expression and rearranging gives

$$\sigma_F = \sqrt{1+\mu'^2}\tau_{\rm max} - \mu'\sigma_{\rm max}.$$

When evaluating the expression in a three-dimensional stress field, it is necessary to solve for the principal stresses by diagonalizing the stress tensor, and then select the greatest and least principal stresses to compute the maximum shear stress $\tau_{\rm max} = (\sigma_1 - \sigma_3)/2$ and the normal stress on planes of maximum shear $\sigma_{\rm max} = (\sigma_1 + \sigma_3)/2$,

$$\sigma_F = \left(\sqrt{\mu'^2+1}\right)\left\{\frac{\sigma_1-\sigma_3}{2}\right\} - \mu'\frac{\sigma_1+\sigma_3}{2}. \quad (13)$$

Acknowledgments. Jeanne Hardebeck, Carl Kisslinger, Andy Michael, Rob Twiss, and Erik Ivins provided constructive reviews. Greg Beroza and David Wald provided their source models. S.J.G. was supported by NSF grant EAR-9628458. R.B. was supported by U.S. Geological Survey NEHRP grant 1434-96-G-2744.

References

Amelung, F., Kinematics of small earthquakes and active tectonics and topography in the San Francisco Bay region, Ph.D. thesis, 97 pp., Univ. Louis-Pasteur, Strasbourg, France, 1996.

Beroza, G. C., Near-source modeling of the Loma Prieta earthquake: Evidence for heterogeneous slip and implications for earthquake hazard, *Bull. Seismol. Soc. Am.*, *81*, 1603-1621, 1991.

Beroza, G. C., and M. D. Zoback, Mechanism diversity of the Loma Prieta aftershocks and the mechanics of mainshock-aftershock interaction, *Science*, *259*, 210-213, 1993.

Bürgmann, R., P. Segall, M. Lisowski, and J. Svarc, Postseismic strain following the 1989 Loma Prieta earthquake from GPS and leveling measurements, *J. Geophys. Res.*, *102*, 4933-4956, 1997.

Byerlee, J. D., Model for episodic flow of high pressure water in fault zones before earthquakes, *Geology*, *21*, 303-306, 1993.

Dieterich, J. H., A constitutive law for rate of earthquake production and its application to earthquake clustering, *J. Geophys. Res.*, *99*, 2601-2618, 1994.

Gross, S. J., Aftershocks of nuclear explosions compared to natural aftershocks, *Bull. Seismol. Soc. Am.*, *86*, 1054-1060, 1996.

Gross, S. J., and C. Kisslinger, Tests of models of aftershock rate decay, *Bull. Seismol. Soc. Am. 84*, 1571-1579, 1994.

Gross, S. J., and C. Kisslinger, Estimating tectonic stress rate and state with Landers aftershocks, *J. Geophys. Res.*, *102*, 7603-7612, 1997.

Harris, R. A., R. W. Simpson, and P. A. Reasenberg, Influence of static stress changes on earthquake locations in southern California, *Nature*, *375*, 221-224, 1995.

Hill, D. P., A note on ambient pore pressure, fault-confined pore pressure, and apparent friction, *Bull. Seismol. Soc. Am. 83*, 583-586, 1993.

Hill, D. P., J. P. Eaton, W. L. Ellsworth, R. S. Cockerham, F. W. Lester, and E. J. Corbett, The seismotectonic fabric of central California, in *Neotectonics of North America: Decade Map 1*, pp. 107-132, Geol. Soc. of Am., Boulder, Colo., 1991.

King, G. C., R. S. Stein, and J. Lin, Static stress changes and the triggering of earthquakes, *Bull. Seismol. Soc. Am.*, *84*, 935-953, 1994.

Kisslinger, C., The stretched exponential function as an alternative model for aftershock decay rate, *J. Geophys. Res.*, *98*, 1913-1922, 1993.

Kostrov, B. V., Crack propagation at variable velocity, *J. Appl. Math. Mech.*, *38*, 551-60, 1974.

Lee, W. H. K., and J. C. Lahr, HYPO71 (revised): A computer program for determining hypocenter, magnitude, and first motion pattern of local earthquakes, *U.S. Geol. Surv. Open File Rep.*, *75-311*, 1-114, 1975.

Lisowski, M., J. C. Savage and W. H. Prescott, The velocity field along the San Andreas Fault in southern California, *J. Geophys. Res.*, *96*, 8369-8389, 1991.

Michael, A. J., W. L. Ellsworth, and D. H. Oppenheimer, Coseismic stress changes induced by the 1989 Loma Prieta, California earthquake, *Geophys. Res. Lett.*, *17*, 1441-1444, 1990.

Nostro, C., M. Cocco, and M. E. Belardinelli, Static stress changes in extensional regimes: An application to southern Apennines (Italy), *Bull. Seismol. Soc. Am.*, *87*, 234-248, 1997.

Ogata, Y., Estimation of the parameters in the modified Omori formula for aftershock sequences by the maximum likelihood procedure, *J. Phys. Earth*, *31*, 115-124, 1983.

Reasenberg, P. A., and R. W. Simpson, Response of regional seismicity to the static stress change produced by the Loma Prieta earthquake, *Science*, *255*, 1687-1690, 1992.

Wald, D. J., D. V. Helmberger, and T. H. Heaton, Rupture model of the 1989 Loma Prieta earthquake from the inversion of strong-motion and broadband teleseismic data, *Bull. Seismol. Soc. Am.*, *81*, 1540-1572, 1991.

Zoback, M. D., and G. C. Beroza, Evidence for near-frictionless faulting in the 1989 (M 6.9) Loma Prieta, California, earthquake and its aftershocks, *Geology*, *21*, 181-185, 1993.

R. Bürgmann, Department of Geology, University of California, Davis, Davis, CA 95616.
(e-mail: burgmann@ymir.ucdavis.edu)

S. J. Gross, CIRES, University of Colorado, Boulder, Campus Box 216 Boulder, CO 80309-0216.
(e-mail: sjg@quake.colorado.edu)

(Received April 17, 1997; revised September 8, 1997; accepted October 21, 1997.)